Surfaces and Interfaces 40 (2023) 103108

Contents lists available at ScienceDirect

Surfaces and Interfaces

journal homepage: www.sciencedirect.com/journal/surfaces-and-interfaces

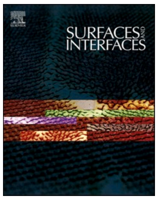

Palladium decorated anatase for photocatalytic partial oxidation of methane to ethane

Jianlong Yang [a], Chao Wang [b], Jialiang Xing [a], Junwang Tang [b,c,*]

[a] Key Lab of Synthetic and Natural Functional Molecule Chemistry of Ministry of Education, the Energy and Catalysis Hub, College of Chemistry and Materials Science, Northwest University; Xi'an 710127, PR China
[b] Department of Chemical Engineering, University College London, Torrington Place, London WC1E 7JE, UK
[c] Industrial Catalysis Center, Department of Chemical Engineering, Tsinghua University, Beijing 100084, China

ARTICLE INFO

Keywords:
Photocatalytic partial oxidation of methane (POM)
Ethane
Pd decorated anatase
Selectivity

ABSTRACT

Photocatalytic partial oxidation of methane (POM) is recognized as a promising, yet challenging technology to realize C_{2+} production. However, the dilemma between the yield and selectivity to C_{2+} products still hinders the commercial application. Here, a strategy for the continuous transformation of methane to ethane with a high activity and a remarkable selectivity is presented when using Pd decorated anatase as the catalyst. The optimized $Pd_{1.8}$-TiO_2 shows a high ethane yield of 40.9 μmol/h, which is 13 times higher than that of bare TiO_2. The ethane selectivity of 80.4% is also comparable to the previous benchmark in POM processes. In situ characterizations reveal that Pd nanoparticle functions as a hole acceptor to facilitate charge separation, thereby significantly improving the performance of POM.

1. Introduction

Large reserves of methane (CH_4) are a promising alternative for a clean fuel and dependable fundamental building block for chemical production [1]. To date, the industrial–scale technology for CH_4 conversion is a two-step process, where CH_4 is firstly transformed into syngas and followed by Fischer-Tropsch synthesis to produce C_{2+} hydrocarbons. However, such a reaction requires huge energy input and strict reaction conditions (e.g., 15–40 atm and 900–1200 K) [2,3]. The low efficiency of carbon-atom utilization causes large greenhouse gas emissions [4]. In contrast, direct C—C bond coupling of CH_4 into ethane (C_2H_6) and further dehydrogenation to ethylene (C_2H_4) are economical, environmentally friendly and important especially in the background of carbon neutrality [5]. The direct CH_4 conversion is initiated by the activation of the C—H bond, which is difficult due to the high C—H bond energy (439 kJ/mol) and low electron affinity (−1.9 eV) [6]. Moreover, the selectivity of desired products is also moderate in CH_4 conversion since the products are thermodynamically more reactive than CH_4 due to the weaker C—H bond in products. There are two main routes for direct C—C bond coupling of CH_4: partial oxidation of CH_4 (POM) and non-oxidative coupling of CH_4 (NOCM). The change in Gibbs free energy of POM (−320 kJ/mol) is much lower than that of NOCM (68.6 kJ/mol), indicating that POM is thermodynamically more favorable than NOCM and can take place under mild conditions [7]. In addition, catalyst deactivation caused by coking is a fatal issue of NOCM [8]. The mostly used oxidant in POM is O_2, leading to the production of C_2H_6, C_2H_4 and H_2O [9]. For example, Mn_2O_3-Na_2WO_4/TiO_2-SiO_2 was used to efficiently convert CH_4 to C_{2-3} with a methane conversion of 22% at 650 °C. However, the C_{2-3} selectivity of 62% was moderate due to the introduction of oxygen and high temperature, which inevitably cause over oxidation [10]. The replacement of O_2 with other oxidants such as CO_2 is one frequent strategy to restrain over oxidation. A recent work used a CaO-based oxide to convert CO_2 and CH_4 to C_2H_6 at 950 °C with C_{2-3} yield of 6.6% [11]. However, the low selectivity of C_2 products remains a major challenge because the product stream is diluted with CO_2, which increases capital investment and energy costs associated with gas separation units for the removal of by-products [12].

Photocatalysis has been regarded as a clean and sustainable strategy

---

Abbreviations: EDX, Energy-dispersive X-ray; ESR, Eelectron spin resonance; HAADF-STEM, High-angle annular dark-field scanning transmission electron microscopy; ICP-AES, Inductively coupled plasma atomic emission spectrometry; NOCM, Non-oxidative coupling of methane; PL, Photoluminescence; POM, Partial oxidation of methane; TEM, Transmission electron microscopy; TPL, Transient-state photoluminescence; UV–vis, Ultraviolet–visible; XPS, X-ray photoeectron spectroscopy; XRD, X-ray diffraction.

* Corresponding author.
E-mail address: junwang.tang@ucl.ac.uk (J. Tang).

https://doi.org/10.1016/j.surfin.2023.103108
Received 5 May 2023; Received in revised form 12 June 2023; Accepted 20 June 2023

to break the C—H bond to drive CH_4 direct conversion under very mild conditions [13]. Integrating photocatalysis and POM may theoretically ameliorate harsh reaction conditions, over-oxidation, and the deposition of coke. In addition, the majority of photocatalytic methane conversion reactions were carried out in batch reactors [14]. Such systems are easy to operate, but it is theoretically hard to avoid over-oxidation as the long residence time in the batch reactor favours the production of thermodynamically more stable overoxidation products (e.g., CO_2). Flow reactors can effectively avoid the overoxidation process due to the readily-controlled reaction time.The flow reactor can also enable to maintain the stable reaction conditions, including feedstock and products concentration. In addition, large-scale operation is only possible in the continuous-flow reactors.

Recently, several relevant works have been reported. CuO_x-Pt-TiO_2 was used for photocatalytic POM in a flow reactor to convert CH_4 to C_2H_6 for the first time, showing the highest yield of C_2 product at 6.8 μmol/h with a moderate selectivity [14]. Later, Ag–AgBr/TiO_2 catalyst was used to selectively convert CH_4 to C_2H_6 under 6 bar pressure, the yield of C_2 product was increased to 35.4 μmol/h [15]. However, the highly selective photocatalysis for valuable C_2 production from methane conversion is still challenging due to the low separation rate of photoinduced carriers in the intrinsic semiconductor and inappropriate residence time of reactants in the reactor.

In this work, an optimized $Pd_{1.8}$-anatase TiO_2 photocatalyst was used for continuous photocatalytic POM in a flow reactor under mild conditions. The C_2H_6 yield achieved is 40.9 μmol/h, which is 13 times higher than that of the pure TiO_2 and comparable to the results of traditional thermal catalysis at high temperatures. The C_2H_6 selectivity of 80.4% is also remarkable owing to the regulation of the gas ratio in the flow reactor. Moreover, diverse characterizations unveil Pd nanoparticles function as photogenerated holes acceptors, increasing the decay lifetime of photoinduced charges, so to largely enhance the activity of $Pd_{1.8}$-TiO_2 catalyst.

2. Main

Pd decorated TiO_2 was synthesized via an in situ photo-deposition method with (1 wt.%) K_2PdCl_4 as the precursor. The resulting catalysts are denoted as Pd_x-TiO_2 (x stands for the weight percentage of loaded Pd species on TiO_2). The morphology of $Pd_{1.8}$-TiO_2 was investigated using transmission electron microscopy (TEM), as shown in Fig. 1A. No obvious Pd particles are observed on $Pd_{1.8}$-TiO_2. The distributed Pd particles were visible in the high-angle annular dark-field scanning transmission electron microscopy (HAADF-STEM) image (Fig. 1B). Energy-dispersive X-ray (EDX) mapping images also show a homogeneous distribution of Pd (Fig. 1C), O (Fig. 1D), and Ti (Fig. 1E) species. The crystalline structures of the photocatalysts were identified by powder X-ray diffraction (XRD), as shown in Fig. 1F. Only anatase TiO_2 (JCPDS no. 84–1272) signals are observed after the deposition of Pd, indicating that the structure of TiO_2 remains unchanged during the photodeposition process [16]. Furthermore, no new diffraction peaks attributed to Pd species are observed, suggesting that the metal species are highly dispersed on the surface of TiO_2. The optical absorption of TiO_2 and various Pd_x-TiO_2 samples were studied by the ultraviolet–visible (UV–vis) absorption spectra (Fig. 1G). TiO_2 exhibits a typical photo-absorption edge at 400 nm. All the photocatalysts display

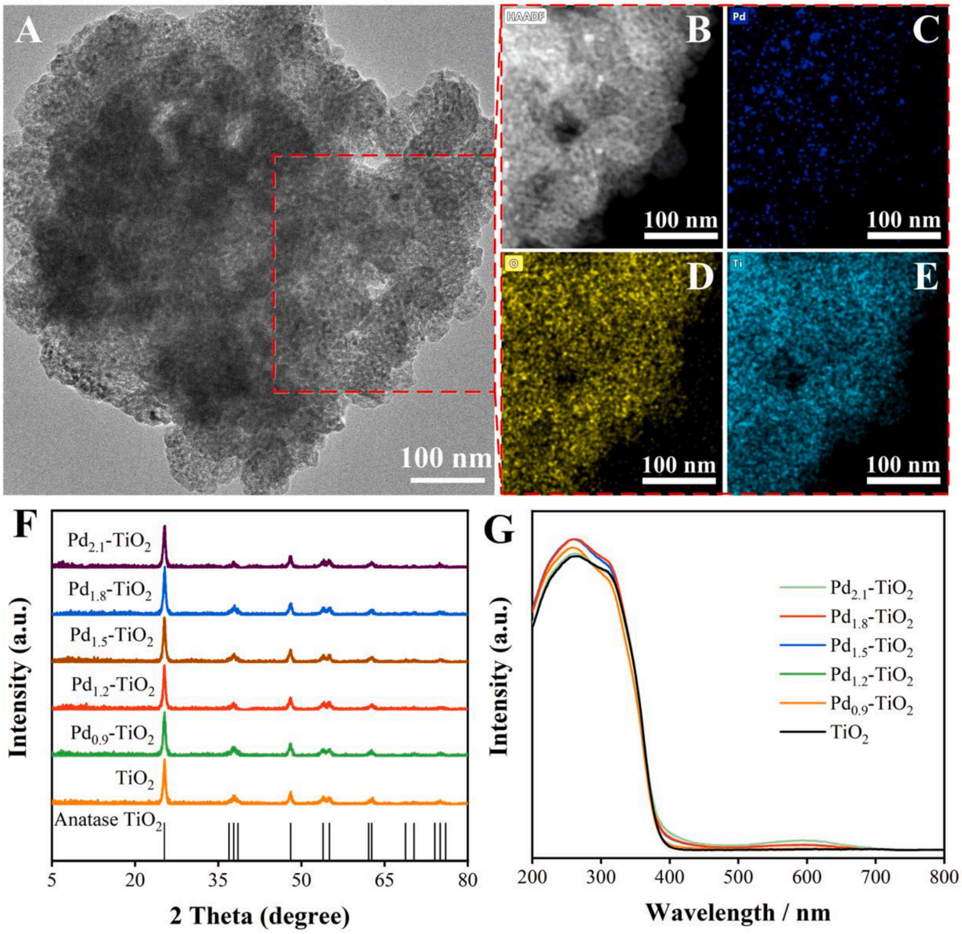

Fig. 1. (A) TEM image of $Pd_{1.8}$-TiO_2, (B) HAADF-STEM of the region in the red dashed box in Fig. 1(A) and the corresponding EDX results of Pd (C), O (D), and Ti (E). (F) XRD patterns and (G) UV–VIS absorption spectra of TiO_2 and Pd_x-TiO_2. (x = 0.9, 1.2, 1.5, 1.8, 2.1).

similar bandgaps around 3.1 eV [17] (Fig. S1). Stability tests indicated that TiO_2 and $Pd_{1.8}$-TiO_2 are stable under the reaction condition (room temperature) (Fig. S2).. The DSC signals at 329 K of TiO_2 and $Pd_{1.8}$-TiO_2 exhibit typical endothermic feature caused by adsorbed water. The broad feature ranging from 750 to 900 K is caused by the transformation of the crystalline phase of TiO_2 [18].

Then, the performance of POM over TiO_2 and Pd_x-TiO_2 photocatalysts was evaluated in a flow reactor. The actual Pd loading was verified by inductively coupled plasma atomic emission spectrometry (ICP-AES). As shown in Fig. 2A, C_2H_6, CO_2 and CO are detected in the products. Bare TiO_2 shows a low C_2H_6 production rate of 2.8 μmol/h, while the production rates of CO_2 and CO are 1.8 μmol/h and 0.2 μmol/h, respectively. The C_2H_6 yield significantly increases from 2.8 μmol/h to 34 μmol/h after loading with 0.9 wt.% Pd. In addition, the selectivity of C_2H_6 increases from 74% to 82.3%. With increasing Pd content, the yield of C_2H_6 further increased to 37.6 μmol/h with 1.2 wt.% Pd content, and reached the highest value over $Pd_{1.5}$-TiO_2 at 41.0 μmol/h. Further increases in Pd loading results in decreased photocatalytic activity, as observed with yields of 40.9 μmol/h and 36.5 μmol/h for $Pd_{1.8}$-TiO_2 and $Pd_{2.1}$-TiO_2, respectively. Meanwhile, the selectivity of the C_2H_6 also exhibits an inverted volcanic trend, with values of 80.8%, 79.7%, 80.4% and 82.1% for $Pd_{1.2}$-TiO_2, $Pd_{1.5}$-TiO_2, $Pd_{1.8}$-TiO_2 and $Pd_{2.1}$-TiO_2. The morphology of $Pd_{2.1}$-TiO_2 was investigated by TEM. As shown in Fig. S3, the yellow circle representing an agglomerated Pd particle with a particle size exceeding 50 nm. Thus, excessive Pd loading causes the aggregation of Pd species, resulting in decreased photocatalytic activity. Based on the results, $Pd_{1.8}$-TiO_2 was selected as the optimized catalyst for subsequent experiments due to its similar C_2H_6 yield compared to $Pd_{1.5}$-TiO_2, but with the higher selectivity. In addition, as shown in Table S1, compared with the reported photocatalysts, the well-designed $Pd_{1.8}$-TiO_2 catalyst shows a high C_2H_6 production rate of 40.9 μmol/h in photocatalytic methane oxidation with a selectivity of 80.4% under mild conditions. The effect of CH_4 to O_2 ratio was then investigated at a total flow rate of 50 mL/min. The CH_4 conversion rates decrease, while the selectivities of C_2H_6 increase as the CH_4 to O_2 ratio increases. The C_2H_6 production rate exhibits a volcanic trend suggesting that O_2 enhances the photocatalytic activity of $Pd_{1.8}$-TiO_2 but also causes severe overoxidation.

To reveal the mechanism behind the excellent activity of $Pd_{1.8}$-TiO_2, the charge transfer behavior of the samples was studied. The in situ Pd 3d XPS results of $Pd_{1.8}$-TiO_2 are shown in Fig. 3A. As shown in the top panel, the dominant XPS signals of $Pd_{1.8}$-TiO_2 in dark at 334.8 and 340.1 eV are attributed to the Pd 3d 3/2 and Pd 3d 5/2 signals, respectively [19,20]. The deconvolution results indicate that the chemical state of Pd species are Pd^0 and Pd^{2+}. Under light irradiation, the binding energy of Pd 3d 3/2 presents a left shift to 335 eV. Such shift of the Pd 3d 3/2 XPS peak to higher binding energy demonstrates Pd species functions as the hole acceptors. The charge transfer behavior was further studied by electron spin resonance (ESR). The ESR signals of TiO_2 in dark and under light irradiation are shown in Fig. S4. No obvious signal is detected over TiO_2 in dark, while strong signals of Ti^{3+} sites at $g = 1.989$ and O^- sites at $g = 2.016$ are observed under light irradiation [21–23]. For $Pd_{1.8}$-TiO_2 (Fig. 3B), either in dark or under light irradiation, no obvious O^- signal is detected. However, the Ti^{3+} signal at $g = 1.989$ is detected under light irradiation, confirming that Pd species function as photogenerated holes acceptor. The charge dynamics of typical samples were investigated by transient-state photoluminescence (TPL). Fig. 3C shows the normalized TPL kinetics of TiO_2 and $Pd_{1.8}$-TiO_2. The TPL decay profiles indicate the decay lifetime of TiO_2 is increased from 4.18 to 5.07 ns by introducing Pd species, providing a charge transfer efficiency of 21% [24]. Besides, photoluminescence (PL) was performed to investigate the recombination of charge carriers in TiO_2 and $Pd_{1.8}$-TiO_2 (Fig. 3D) [25]. The PL intensities of TiO_2 is significantly lower than that of $Pd_{1.8}$-TiO_2, which agrees with the trend in the photocatalytic activity. Since low PL intensity corresponds to low recombination rate of photogenerated charges, the lower PL intensity suggests a smaller recombination rate of photogenerated charges in $Pd_{1.8}$-TiO_2. The function of Pd species as a hole acceptor was further consolidated by transient photocurrent response (Fig. 3E). In comparison to TiO_2, $Pd_{1.8}$-TiO_2 exhibits a higher photocurrent density due to the efficient transfer of holes to Pd nanoparticles. This high kinetic efficiency initially leads to an accumulation of holes near the photoelectrode, thereby enhancing the electron-hole recombination at the interface of the photoelecrode and electrolyte. As a result, the photocurrent density initially decreases until it reaches a stable state. In contrast, TiO_2 demonstrates poor charge carrier separation ability, resulting in a small photocurrent. Based on the above results, a probable mechanism of photocatalytic POM over $Pd_{1.8}$-TiO_2 is proposed (Fig. 3F). Upon light irradiation, electrons of TiO_2 are excited from the VB to its CB, while the photogenerated holes transfer to Pd particles, thereby efficiently suppressing the recombination of photo charges. A C—H bond in CH_4 molecules is cleaved by the holes to form $\cdot CH_3$ and H^+. The spontaneous combination of $\cdot CH_3$ formed C_2H_6. O_2 could be reduced by electrons to form O^{2-}, and the H^+ could be removed by O^{2-} to form water.

3. Conclusion

In summary, a continuous photocatalytic POM reaction under mild conditions has been successfully achieved using the Pd-decorated TiO_2 catalyst in a flow reactor. The optimized $Pd_{1.8}$-TiO_2 catalyst produces C_2H_6 at a rate of 40.9 μmol/h, which is 13 times higher than that of the pure TiO_2, together with an advantageous C_2H_6 selectivity of 80.4%. The Pd nanoparticles function as the photogenerated hole acceptor, prolonging the lifetime of photocharges, so as to largely enhance the

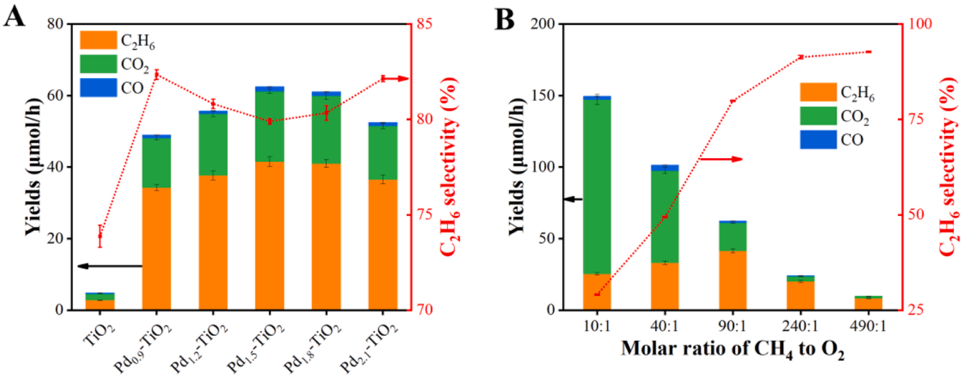

Fig. 2. (A) The product distribution and C_2H_6 product selectivity over TiO_2 and Pd_x-TiO_2 ($x = 0.9, 1.2, 1.5, 1.8, 2.1$). (B) The product distribution and C_2H_6 product selectivity over $Pd_{1.8}$-TiO_2 with different molar ratios of CH_4 to O_2. Reaction conditions: 50 mg catalyst, 365 nm light irradiation, under room temperature and 0.1 MPa, with a flow rate of 50 ml/min, molar ratio of CH_4 to O_2 is 90:1, the data were recorded at 30th minute.

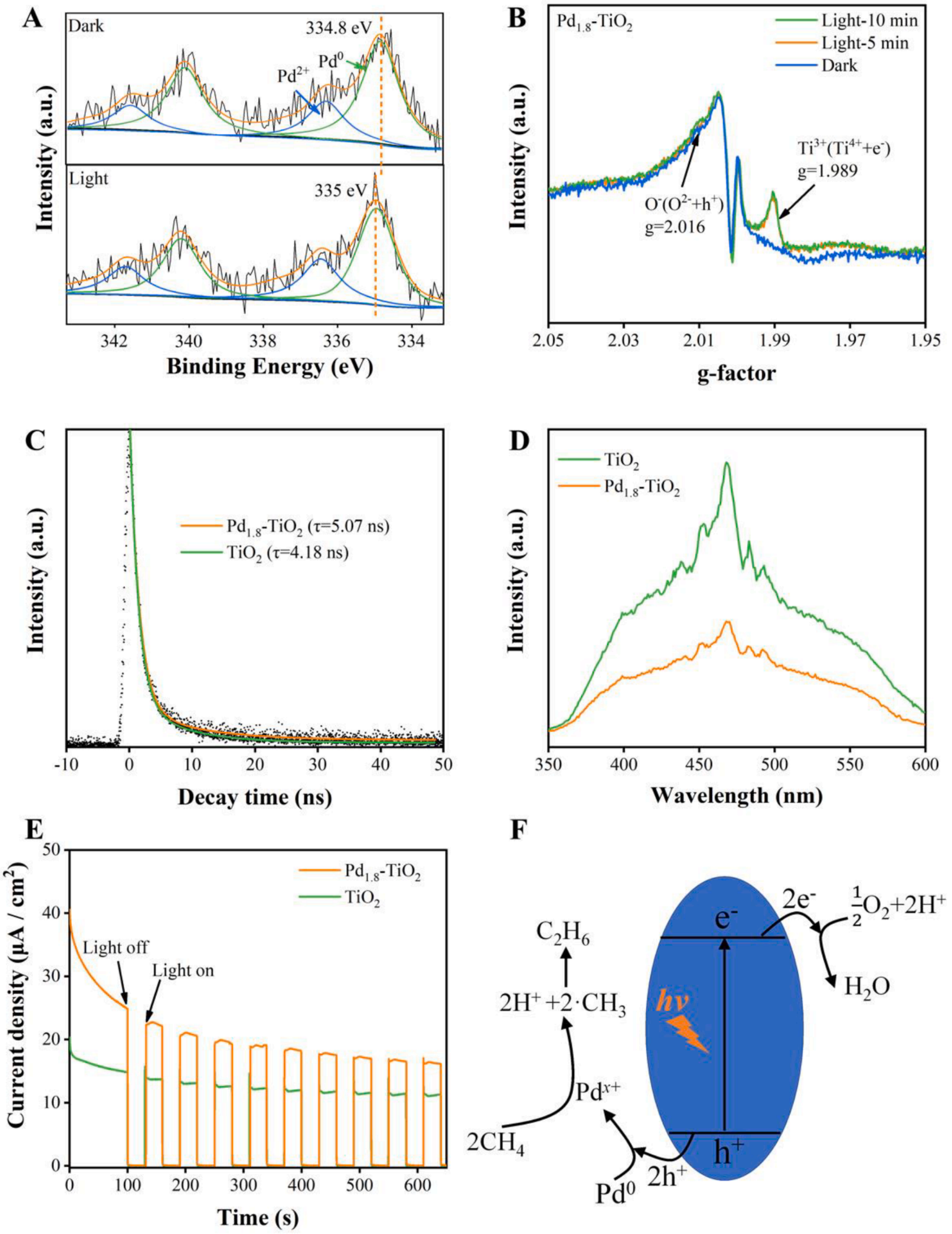

Fig. 3. (A) Pd 3d XPS spectra and (B) EPR spectra under 100 K of $Pd_{1.8}$-TiO_2 in dark and under light irradiation. (C) Time-resolved photoluminescence (TPL) spectra, (D) Photoluminescence (PL) spectra, and (E) I-T curves of TiO_2 and $Pd_{1.8}$-TiO_2. (F) Proposed reaction mechanism of photocatalytic POM on Pd decorated TiO_2.

activity of the $Pd_{1.8}$-TiO_2 catalyst. Overall, this work provides an effective and green route toward continuous methane conversion to value-added products.

4. Methods

4.1. Chemicals and materials

Titanium dioxide (TiO_2, 60 nm, anatase, 99.8%, Alfa Aesar), potassium tetrachloropalladate (II) solution (1 wt.% Pd) were applied in the experimental studies.

4.2. Preparation of Pd_x-TiO_2

300 mg TiO_2 was suspended in 30 mL aqueous methanol solution (10 vol.%), where a certain amount of K_2PdCl_4 was then added. The suspensions were sealed and irradiated for 4 h after purging with ultrapure Ar for 30 min. Then, the products were washed with DI water and collected by centrifugation. The obtained products were named Pd_x-TiO_2, where x represented the wt. percentage of Pd to TiO_2 substrates.

4.3. Characterization

TEM images were acquired via FEI Talos F200X, equipped with an Energy-dispersive X-ray Detector. XRD patterns were obtained on a Bruker D8 Advance fitted with a solid-state X' Celerator detector (2.2 kW) using Cu Kα radiation from 5 to 80°. The UV–Vis absorption spectra were acquired using a Shimadzu UV 3600 plus spectrophotometer with $BaSO_4$ as the reference. In-suit XPS was performed on a Thermo Scientific ESCALAB 250Xi system with an Al Kα source, where a 365 nm Led light was utilized as the excitation source. All XPS spectra were calibrated using C 1s line at 284.6 eV. The contents of Pd species were measured by an ICP-MS (Agilent 7900). Photoluminescence and transient-state photoluminescence were collected on an FLSP920 spectrofluorometer. The excitation and emission wavelength of TPL were 310 and 470 nm, respectively. The electron spin resonance (ESR) measurements were carried out on a Bruker E500–9.5/12 spectrometer operating at the X-band frequency at room temperature, where a 365 nm LED was applied as the irradiation source. TGA-DSC was performed on a NETZSCH STA449C under Ar atmosphere

4.4. Photocatalytic test

50 mg sample powder was suspended in 50 mL water and filtered with a nylon membrane (diameter 35 mm) to produce a uniform film. The film was placed on the top-irradiated flow reactor with a temperature probe. For each experiment, the system was purged with Ar (50 mL·min^{-1}) for 30 min. Subsequently, the reactor was irradiated by a LED light source (365 nm Beijing Perfect Light, PLS-LED 100B) with a CH_4 flow rate of 50 ml/min. The outlet gasses were detected by an SP-3420A GC equipped with a thermal conductivity detector (TCD) and a flame ionization detector (FID).

4.5. Calculation of selectivity

The selectivity for C_2H_6 was calculated as below:

$$C_2H_6 \text{ selectivity} = \frac{2 \times n(C_2H_6)}{2 \times n(C_2H_6) + n(CO_2) + n(CO)}$$

Data availability

The authors declare that the data supporting the findings of this study is available in the main text or the supplementary materials.

CRediT authorship contribution statement

Jianlong Yang: Investigation, Formal analysis, Writing – original draft, Visualization. **Chao Wang:** Formal analysis, Writing – original draft, Visualization. **Jialiang Xing:** Formal analysis, Writing – original draft. **Junwang Tang:** Supervision, Conceptualization, Writing – review & editing, Funding acquisition.

Declaration of Competing Interest

The authors declare that they have no known competing financial interests or personal relationships that could have appeared to influence the work reported in this paper.

Acknowledgments

All authors acknowledge funding from UK EPSRC (EP/ S018204/2), and Royal Society Leverhulme Trust Senior Research Fellowship (SRF \R1\21000153). J. T. also acknowledges the NSFC project (Grant No: 22250710677) and Beijing Municipal Project (C2022007). C.W. acknowledges the UCL Dean's prize and China CSC scholarship.

Supplementary materials

Supplementary material associated with this article can be found, in the online version, at doi:10.1016/j.surfin.2023.103108.

References

[1] N.J. Gunsalus, A. Koppaka, S.H. Park, et al., Homogeneous functionalization of methane, Chem. Rev. 117 (2017) 8521–8573.

[2] W.-J. Jang, J.-O. Shim, H.-M. Kim, et al., A review on dry reforming of methane in aspect of catalytic properties, Catal. Today 324 (2019) 15–26.

[3] A. Iulianelli, S. Liguori, J. Wilcox, et al., Advances on methane steam reforming to produce hydrogen through membrane reactors technology: a review, Catal. Rev. 58 (2016) 1–35.

[4] X. Guo, G. Fang, G. Li, et al., Direct, nonoxidative conversion of methane to ethylene, aromatics, and hydrogen, Science 344 (2014) 616–619.

[5] X. Meng, X. Cui, N.P. Rajan, et al., Direct methane conversion under mild condition by thermo-, electro-, or photocatalysis, Chem 5 (2019) 2296–2325.

[6] L. Meng, Z. Chen, Z. Ma, et al., Gold plasmon-induced photocatalytic dehydrogenative coupling of methane to ethane on polar oxide surfaces, Energy Environ. Sci. 11 (2018) 294–298.

[7] X. Wang, N. Luo, F. Wang, Advances and challenges of photocatalytic methane C—C coupling, Chin. J. Chem. 40 (2022) 1492–1505.

[8] S.P. Singh, A. Anzai, S. Kawaharasaki, et al., Non-oxidative coupling of methane over Pd-loaded gallium oxide photocatalysts in a flow reactor, Catal. Today 375 (2021) 264–272.

[9] G.E. Keller, M.M. Bhasin, Synthesis of ethylene via oxidative coupling of methane: I. Determination of active catalysts, J. Catal. 73 (1982) 9–19.

[10] P. Wang, G. Zhao, Y. Wang, et al., $MnTiO_3$-driven low-temperature oxidative coupling of methane over TiO_2-doped Mn_2O_3-Na_2WO_4/SiO_2 catalyst, Sci. Adv. 3 (2017), e1603180.

[11] Y. Zhang, Y. Cho, A. Yamaguchi, et al., CO_2 oxidative coupling of methane using an earth-abundant CaO-based catalyst, Sci. Rep. 9 (2019) 15454.

[12] J. Liu, J. Yue, M. Lv, et al., From fundamentals to chemical engineering on oxidative coupling of methane for ethylene production: a review, Carbon Resour. Convers. 5 (2022) 1–14.

[13] X. Li, C. Wang, J. Tang, Methane transformation by photocatalysis, Nat. Rev. Mater. 7 (2022) 617–632.

[14] X. Li, J. Xie, H. Rao, et al., Platinum- and CuO_x -decorated TiO_2 photocatalyst for oxidative coupling of methane to C_2 hydrocarbons in a flow reactor, Angew. Chem. 59 (2020) 19702–19707.

[15] C. Wang, X. Li, Y. Ren, et al., Synergy of Ag and AgBr in a pressurized flow reactor for selective photocatalytic oxidative coupling of methane, ACS Catal. 13 (2023) 3768–3774.

[16] D. Li, Y. Liu, W. Shi, et al., Crystallographic-orientation-dependent charge separation of $BiVO_4$ for solar water oxidation, ACS Energy Lett. 4 (2019) 825–831.

[17] G. Liu, H.G. Yang, J. Pan, et al., Titanium dioxide crystals with tailored facets, Chem. Rev. 114 (2014) 9559–9612.

[18] Z. Zhu, S. Wu, Y. Long, et al., Phase-transition kinetics of silicon-doped titanium dioxide based on high-temperature X-ray-diffraction measurements, J. Solid State Chem. 303 (2021), 122544.

[19] A.F. Lee, J.N. Naughton, Z. Liu, et al., High-pressure XPS of crotyl alcohol selective oxidation over metallic and oxidized Pd(111), ACS Catal. 2 (2012) 2235–2241.

[20] S. Chen, S. Li, R. You, et al., Elucidation of active sites for CH_4 catalytic oxidation over Pd/CeO_2 via tailoring metal–support interactions, ACS Catal. 11 (2021) 5666–5677.

[21] D.C. Hurum, A.G. Agrios, S.E. Crist, et al., Probing reaction mechanisms in mixed phase TiO_2 by EPR, J. Electron. Spectrosc. Relat. Phenomena 150 (2006) 155–163.

[22] P. Stefanov, S. Todorova, A. Naydenov, et al., On the development of active and stable Pd–Co/γ-Al_2O_3 catalyst for complete oxidation of methane, Chem. Eng. J. 266 (2015) 329–338.

[23] Tsutomu Hirakawa, Hiroshi Kominami, Bunsho Ohtani, et al., Mechanism of photocatalytic production of active oxygens on highly crystalline TiO_2 particles by means of chemiluminescent probing and ESR spectroscopy, J. Phys. Chem. B 105 (2003) 6993–6999.

[24] Y. Wang, Y. Qu, B. Qu, et al., Construction of six-oxygen-coordinated single Ni sites on g-C_3N_4 with boron-oxo species for photocatalytic water-activation-induced CO_2 reduction, Adv. Mater. 33 (2021), e2105482.

[25] J. Bian, J. Feng, Z. Zhang, et al., Dimension-matched zinc phthalocyanine/$BiVO_4$ ultrathin nanocomposites for CO_2 reduction as efficient wide-visible-light-driven photocatalysts via a cascade charge transfer, Angew. Chem. Int. Ed. 58 (2019) 10873–10878.